Catalysis
Science &
Technology

Mechanistic study of the ceria supported, Re-catalyzed deoxydehydration of vicinal OH groups

SCHOLARONE™
Manuscripts

Mechanistic study of the ceria supported, Re-catalyzed deoxydehydration of vicinal OH groups

Yongjie Xi[#], Wenqiang Yang[#], Salai Cheettu Ammal[#], Jochen Lauterbach[#], Yomaira Pagan-Torres[$] and Andreas Heyden[#,*]

[#]Department of Chemical Engineering, University of South Carolina, 301 South Main Street, Columbia, South Carolina 29208, United States

[$]Department of Chemical Engineering, University of Puerto Rico-Mayaguez Campus, Mayaguez, Puerto Rico 006814-9000, United States

ABSTRACT

Deoxydehydration (DODH) is an emerging biomass deoxygenation process whereby vicinal OH groups are removed. Based on DFT calculations and microkinetic modeling, we seek to understand the mechanism of the Re-catalyzed deoxydehydration supported on $CeO_2(111)$. In addition, we aim at understanding the promotional effect of Pd in a heterogeneous ReO_x-Pd/CeO_2 DODH catalyst system. We disentangle the contribution of the oxide support, the oxide-supported single ReO_x species, and a co-adsorbed Pd promoter that has no direct interaction with the Re species. In the absence of a nearby Pd cluster, a Re site is able to reduce subsurface Ce-ions of a hydroxylated $CeO_2(111)$ surface, leading to a catalytically active Re +6 species. The effect of Pd is twofold: (*i*) Pd catalyzes the hydrogen dissociation and spillover onto CeO_2, which is an indispensable process for the regeneration of the Re catalyst, and (*ii*) Pd adsorbed in close proximity to Re on $CeO_2(111)$ facilitates the oxidation of Re to a +7 oxdiation state, which leads to an even more active Re species than the Re +6 site present in the absence of Pd. The latter promotional effect of Pd (and change in oxidation state of Re) disappears with increasing Pd-Re distance and in the presence of oxygen defects on the ceria support. Under these conditions, the ReO_x-Pd/CeO_2 catalyst system exhibits appreciable activity consistent with recent experiments. The established mechanism and role of various species in the catalyst system

help to better understand the deoxydehydration catalysis. Also, the importance of the Re oxidation state and the identified oxidation state modification mechanisms suggest a new pathway for tuning the properties of metal-oxide supported catalysts.

KEYWORDS: deoxydehydration; single-atom catalysis; ceria; biomass conversion; oxidation state.

---

*Corresponding author contact: email: heyden@cec.sc.edu phone: +1-803-777-5025

1. Introduction

Utilization of biomass by transforming it into fuels and chemicals is a promising approach for achieving global sustainability.[1, 2] Compared to fossil resources, biomass-derived raw materials are usually oxygen-rich, necessitating the reduction of the oxygen content to valorize biomass. Various deoxygenation systems have been developed to convert biomass to value-added chemicals, such as dehydration,[3] hydrodeoxygenation,[4] decarbonylation,[5] and decarboxylation.[6] In the quest for improved deoxygenation catalysts, there is a flurry of interest in the deoxydehydration process, which is the removal of two vicinal OH groups, converting a vicinal diol to an alkene.[7] In Cook and Andrew's seminal work of DODH in 1996, they reported a homogeneous Re catalyst with PPh_3 as the reductant to regenerate the catalyst.[8] As a commercial organometallic compound, methyltrioxorhenium (MTO), has been extensively explored as a model DODH catalyst.[9, 10] Later, V[11] and Mo-based[12] homogeneous DODH catalysts were also developed as replacements for the high cost rhenium compounds. The first heterogeneous DODH catalyst, ReO_x supported on activated carbon, was reported in 2013, albeit with leaching of catalyst into the solvent and fast activity loss.[13] Most of the subsequently reported heterogeneous DODH catalysts were also based on Re, supported on ceria[14] or titania.[15] Very recently, a non-Rhenium DODH catalyst, MoO_x/TiO_2 was reported.[16] Commonly held perceptions on the mechanism of a DODH process involve the following steps: (1) breaking of the two diol OH-bonds by the catalyst and forming a diolate species and an adsorbed H_2O. The water molecule can usually desorb readily. This is also called the condensation step. (2) The desorption of the alkene from the low valent catalyst, leaving an additional oxygen on the catalyst and forming a high valent species, known as the extrusion step. (3) The regeneration of the catalyst by a reductant, that is the reduction step. PPh_3,[8] Na_2SO_3,[17] and alcohols[18] are commonly used reductants in the DODH reaction. Efforts have also been made for using more practical reductants such as H_2[9] and CO.[19]

Recently, Tomishige et al. reported a CeO_2 supported ReO_x DODH catalyst for which the Re species are atomically dispersed.[14, 20] Through screening of various oxide supported Re catalysts, they found that CeO_2 is the best support of Re while the presence of the co-adsorbed palladium can promote the activity and selectivity of the catalyst significantly. Using H_2 as reductant, a ReO_x-Pd/CeO_2 (Re=2 wt%, Pd/Re=0.25) catalyst exhibited a remarkable selectivity for the conversion of cis-1,4-anhydroerythritol

(AE) to dihydrofuran (DHF), which is further hydrogenated to tetrahydrofuran (THF). The active site was proposed to be monomeric Re species stabilized on the CeO_2 support. The turnover frequency (TOF) per Re atom at 443 K was calculated to be ~0.083/s, one order of magnitude larger than typical of homogeneous catalysts at the same temperature.[20] While not all Re species are monomeric, it has been proposed that only isolated Re species are catalytically active. It has also been estimated that about 90% of the Re did not interact with Pd and that the Pd-bound Re species are inactive. The coordination number of Pd−Pd is about 3, implying that Pd species are highly dispersed.[14]

As a common practice to improve the catalytic performance, a small concentration of impurity elements are added to a catalyst, known as promoter.[21] For example, potassium is used as a promoter for ammonia synthesis[22] and Fischer–Tropsch synthesis.[23] While literature reports of promotional phenomena in catalysis are abundant, detailed mechanistic insights have been rare.[24-28] Concerning the ReO_x-Pd/CeO_2 DODH catalyst, it is intriguing to understand the behavior of the Pd promoter. In particular, how does the co-adsorbed Pd modifies the properties of the monomeric Re without forming chemical bonds with Re remains an open question.

In the present study, we determine the energy profile of various reaction pathways and unravel the promotional effect of Pd using density functional theory (DFT). Through *ab initio* thermodynamics calculations, we determined the structure of the monomeric Re species. Following the experimental condition, we also used AE as a substrate molecule to examine the catalytic DODH reaction on ReO_x/CeO_2, which was compared with that of ReO_x-Pd/CeO_2. Since the DHF hydrogenation to form THF is a fast step and well-understood, we did not include this step in our investigation. Next, we developed a microkinetic model (MKM) to gain further insights into the reaction mechanism. A novel pathway of ReO_x reduction by H_2 is proposed that is distinct from those on homogeneous catalysts. To our knowledge, this is the first systematic study of the mechanism of the heterogeneous DODH reaction. Considering that Ce has localized 4f orbitals, it is possible to count[29] the electron transfer from the adsorbed species to the CeO_2 support and to assign the oxidation state of the supported species. Based on the analysis of the Re oxidation state, we propose an oxidation state modification mechanism: the presence of Pd can change the oxidation state of nearby Re via the CeO_2 substrate. We finally extend the discussion to the effect of

oxygen vacancies in the ceria support, Pd cluster size, and other noble metal clusters like Au.
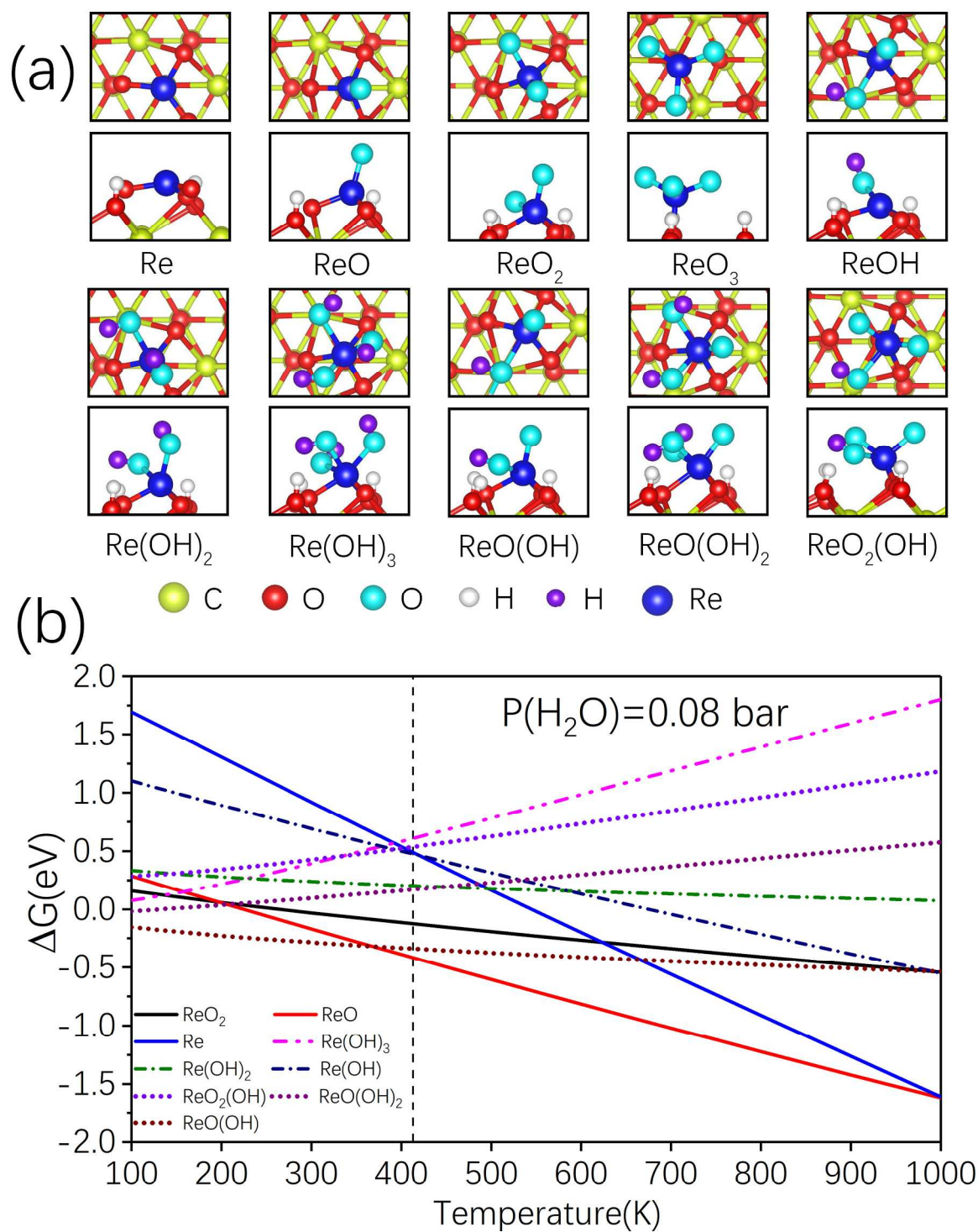
Figure 1 a. Optimized structures of various $ReO_x(OH)_y$ species adsorbed on hydroxylated CeO_2. **b.** The Gibbs free energies of $ReO_x(OH)_y$ species relative to ReO_3 with a hydrogen partial pressure of 80 bar and water

partial pressure of 0.08 bar, respectively. The free energy of $ReO_x(OH)_y$ relative to ReO_3 is balanced by adding H_2 and H_2O, e.g. $\Delta G(ReO_2) = G(ReO_3) + G(H_2) - G(ReO_2) - G(H_2O)$.

2. Methods

2.1 First Principles Methods

First-principles calculations were performed using periodic density functional theory (DFT), as implemented in the Vienna Ab initio Simulation Package (VASP 5.4.1).[30, 31] The spin-polarized generalized gradient approximation (GGA) with the PBE functional was used to treat exchange−correlation effects. A plane wave basis set with a cutoff energy of 500 eV was selected to describe the valence electrons. The electron−ion interactions were described by the projector augmented wave (PAW)[32, 33] method. The Brillouin zone integration was performed with a 2×2×1 Monkhorst−Pack[34] (MP) k-mesh and Gaussian smearing (σ=0.05 eV). An effective Hubbard U value of 5.0 eV was used to describe the strong on-site Coulomb repulsion of the Ce 4f electrons, following previous research.[35] To confirm our DFT+U results, we performed for selected species calculations with the Heyd, Scuseria, and Enrzerhof (HSE06) hybrid functional.[36] We used Grimme's DFT-D3[37] scheme to include the van der Waals interactions semi-empirically. The SCF and force convergence criteria for structural optimization were set to 1×10^{-6} eV and 0.01 eV/Å, respectively. The climbing image nudged elastic band (CI-NEB)[38] and dimer methods[39, 40] were used to optimize the transition state structures. The optimized conventional cell of ceria with a lattice parameter of 3.871 Å was adopted to construct the oxygen terminated[41] $CeO_2(111)$ surface. A (3×2√3) supercell with four O-Ce-O trilayers and 15 Å vacuum slab (Figure S1a and S1b) was used to describe the ceria support during the catalytic process. Solvation effects are not explicitly considered in our calculations due to difficulties in modeling solvation effects for processes at solid-liquid interfaces[42]. Fortunately, the DODH reaction has been found to occur most favorably in 1,4-dioxane which is a non-polar solvent that displays often only a minor influence on a catalyst's activity[43, 44], justifying our approach of initially neglecting direct solvent effects.

2.2 Microkinetic Model

Harmonic transition state theory was used to calculate all elementary rate constants of surface

processes. Collision theory with a sticking coefficient of 1 was used to estimate the rate constants for adsorption processes. While the sticking coefficient may not be 1 in liquid phase reactions, the overall kinetics is hardly affected by the choice of sticking coefficient since the adsorption steps are not rate-controlling but in quasi-equilibrium (*vide infra*). Details of the formulation is provided in the electronic supplementary information. We used typical experimental reaction conditions in our models. The partial pressures (chemical potentials) of AE and DHF were estimated using COSMOtherm[45] (ESI). A H_2 partial pressure of 80 bar was used. The experiments were performed with water solvent, as well as non-water solvent such as 1,4-dioxane. The latter is the optimal experimental condition and is also used to investigate the reaction pathways in the present study. Nonetheless, the presence of water is unavoidable under 1,4-dioxane solvent conditions since small amounts of water are commonly found in gas (hydrogen) streams and since the DODH reaction itself produces water. We approximate the water partial pressure for reactions in 1,4-dioxane solvent as being 0.1% of the H_2 pressure, i.e., 0.08 bar (low water partial pressure scenario). We use the equilibrium water vapor pressure at 413 K, i.e., 3.56 bar, for reactions in liquid water (high water partial pressure scenario). The calculated rate constants are tabulated in Tables S1 and S2. After obtaining the rate constants of each elementary step, we developed a Master equation of probability densities for the system to occupy each discrete state and solved for the steady-state solution. Here, the probability densities are also referred to as surface coverage θ. We solved the Master equation using the BzzMath[46] library. The reaction rate (turnover frequency) of each pathway was calculated using the obtained surface coverages. The apparent activation energy (E_{app}) was calculated from the overall rates over a temperature range of 383−443 K using the expression

$$\mathrm{E}_{app} = RT^2 \left(\frac{\partial \ln r}{\partial T} \right)_{P,y_i} \qquad (1)$$

where the total pressure (P) and the mole fraction of species i in the reaction mixtures (y_i) were kept constant.

The reaction order (α_i) with respect to species i at a specific temperature (T) is calculated by varying the partial pressure of the species (P_i) using the relation

$$\alpha_i = \left(\frac{\partial \ln r}{\partial \ln P_i} \right)_{T, P_{j \neq i}} \quad (2).$$

To identify rate controlling steps and states in the microkinetic models, we also perform a Campbell's degree of kinetic (KRC) and thermodynamic (TRC)[47, 48] rate control analysis.

$$KRC_i = \left(\frac{\partial \ln r}{\partial \ln k_i} \right)_{K_i, k_{j \neq k_i}} \quad (3)$$

where K_i is the equilibrium constant of step i.

$$TRC_n = \left(\frac{\partial \ln r}{\partial \left(-\frac{G_n}{k_B T} \right)} \right)_{G_{m \neq n}, G_i^{TS}} \quad (4)$$

where G_n is the free energy of adsorbate n and G_i^{TS} is the free energy of the tranision state i, respectively.

2.3 Construction of Atomistic Models

Based on the $(3 \times 2\sqrt{3})$ $CeO_2(111)$ surface model, we built the atomistic models for ReO_x-Pd/CeO_2 and ReO_x-Pd/CeO_2 catalysts by unravelling the structure of the ReO_x species. The hydrogen pressure in Tomishige's study was high, which can be indicative of the formation of hydroxyls on ceria under reaction conditions.[49] Indeed, our calculations suggest that the adsorption of hydrogen on ceria is favorable with an exergonicity of -1.99 eV per H_2 at full hydrogen coverage (Figure S1c). The high exergonicity of hydrogen adsorption can be attributed to the large electron affinity of ceria caused by the low-lying 4f states of Ce^{4+}.[50] As such, we adopt the fully-hydrogenated $CeO_2(111)$ surface to construct a model of the DODH catalyst. Next, we examined the interaction of Re with ceria. We found that a Re atom can bind with three oxygen atoms on the pristine $CeO_2(111)$ surface either above a surface O or a surface Ce atom (Figure S2a, b). The former configuration is 4.71 eV more stable than the later and was adopted for subsequent calculations. To model the atomically dispersed Re species on ceria under reaction condition, we first replaced three H atoms (released as 3/2 H_2) from the fully-hydrogenated $CeO_2(111)$ with one Re, which is exergonic by 4.5 eV. The $CeO_2(111)$ supported Re can accommodate some amount of oxygen atoms, forming Re oxide. In the presence of H_2, the Re oxide can also be hydrogenated to

$ReO_x(OH)_y$. We found that x+y can be in the range of 0 to 3; additional O or OH lead to the detachment of $ReO_x(OH)_y$ from the $CeO_2(111)$ surface. The optimized structures of various CeO_2 supported $ReO_x(OH)_y$ species are displayed in Figure 1a. We evaluated the thermodynamic stability of $ReO_x(OH)_y$ species at a fixed pressure of H_2 and H_2O, with the temperature varying from 100 to 1000 K. The relative stability of $ReO_x(OH)_y$ in the low water partial pressure case, corresponding to favorable experimental conditions, is presented in Figure 1b. ReO is found to be the energetically most stable species at 413 K while ReO(OH) and ReO_2 are 0.07 eV and 0.29 eV higher in energy than ReO, respectively, despite the fact that ReO(OH) is the most stable form of isolated Re sites on ceria at 413 K in our high water partial pressure scenario (Figure S3). The free energies of other species are well above these three species at 413 K. In the ensuing investigation, we focused our attention on the low water partial pressure scenario and the model of the ReO/CeO_2 catalyst (**Model-A**) is shown in Figure 2a, c. The model of the $ReO-Pd/CeO_2$ catalyst (**Model-B**, Figure 2b, d) is constructed by replacing 3 H atoms with a Pd_4 cluster in tetrahedral conformation, adsorbed on its most stable adsorption site on the ceria surfaced (**Model-A,** Figure S2c, d). Here, any direct interaction between Re and Pd is avoided. The replacement of 3 H atoms with Pd_4 is exergonic by 2.21 eV. Here, we also examined an adsorption configuration of a ReO species on a Pd_4 cluster (Figure S2e) rather than the ReO species and the Pd_4 cluster being separated as is the case in **Model-B**. Due to the oxophilic nature of Re, the Pd_4-loaded ReO is 2.13 eV higher in energy than **Model-B**. Next, we verified the relative stability of ReO, ReO(OH), and ReO_2 at 413 K for ReO_x-Pd/CeO_2, concluding that Re-O remains the most stable species in the presence of Pd, with ReO(OH) and ReO_2 being 0.64 and 1.10 eV higher in energy, respectively. Therefore, the adoption of **Model-B** as the atomistic model $ReO-Pd/CeO_2$ is justified.
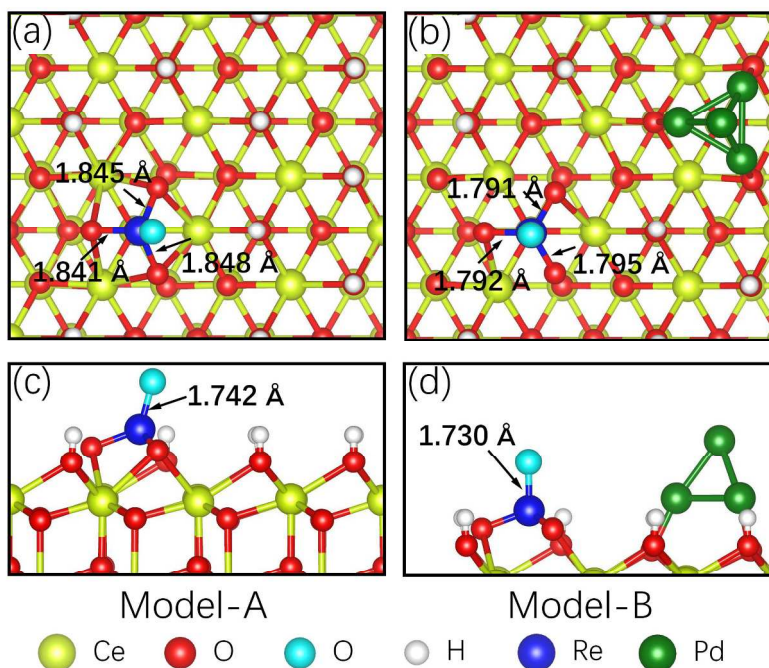
Figure 2. Top view (**a**) and side view (**c**) for the model of ReO/CeO$_2$(**Model-A**); Top view (**b**) and side view (**d**) for the model of ReO-Pd/CeO$_2$ (**Model-B**). Re-O bond lengths are labeled.

3. Results
3.1 Proposed reaction pathway

Having established an atomistic model of ReO/CeO$_2$ and ReO-Pd/CeO$_2$ catalysts, we performed a mechanistic study of AE deoxydehydration over the two catalysts. As mentioned, an additional oxygen will be left on the catalyst after the DODH reaction. In the present case, ReO will be converted to ReO$_2$, making it necessary to regenerate the catalyst by reducing the ReO$_2$ with hydrogen. In principle ReO$_2$ can be directly reduced by H$_2$, yet the activation energy can be high (*vide infra*), inconsistent with the high catalytic activity of ReO-Pd/CeO$_2$. Therefore, we proposed an alternative pathway for ReO$_2$ reduction by the hydrogen of the hydroxyls on ceria displayed in Figure 3, which is also applicable in **Model-B** where a co-adsorbed Pd cluster is included**.** Steps **I** and **II** correspond to the aforementioned condensation step of the DODH. Step **III** is the desorption of the alkene (the facile desorption of water is also included). In step **IV**, a hydrogen atom (H$_a$) migrates to a neighboring oxygen bonded to Re, creating a hydrogen vacancy (H$_{vac}$) on the hydroxylated CeO$_2$. Next, another hydrogen (H$_b$) replenishes the vacancy created by the removal of H$_a$ (step **V**), which is followed by the formation of water (step **VI**). The catalytic cycle is closed when H$_2$O desorbs (VII) and the two hydrogen vacancies are replenished by dissociative

10

adsorption of H_2 (step **VIII**).
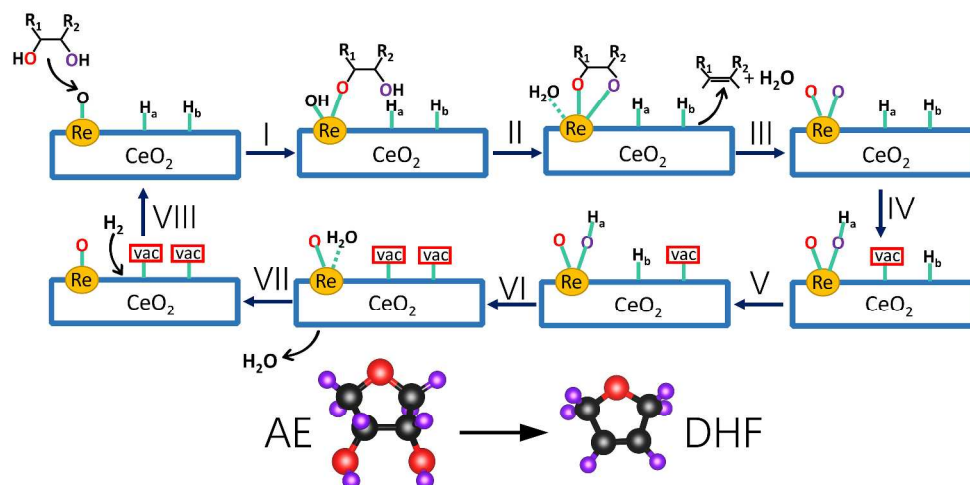
Figure 3. Schematics of the deoxydehydration of vicinal diol over ceria supported Re-O, followed by catalyst regeneration through a surface hydrogen migration process. Reaction steps are labelled as **I-VIII**. Stable configurations of AE and DHF are presented. Here, carbon, oxygen, and hydrogen atoms are represented in black, red, and purple, respectively.
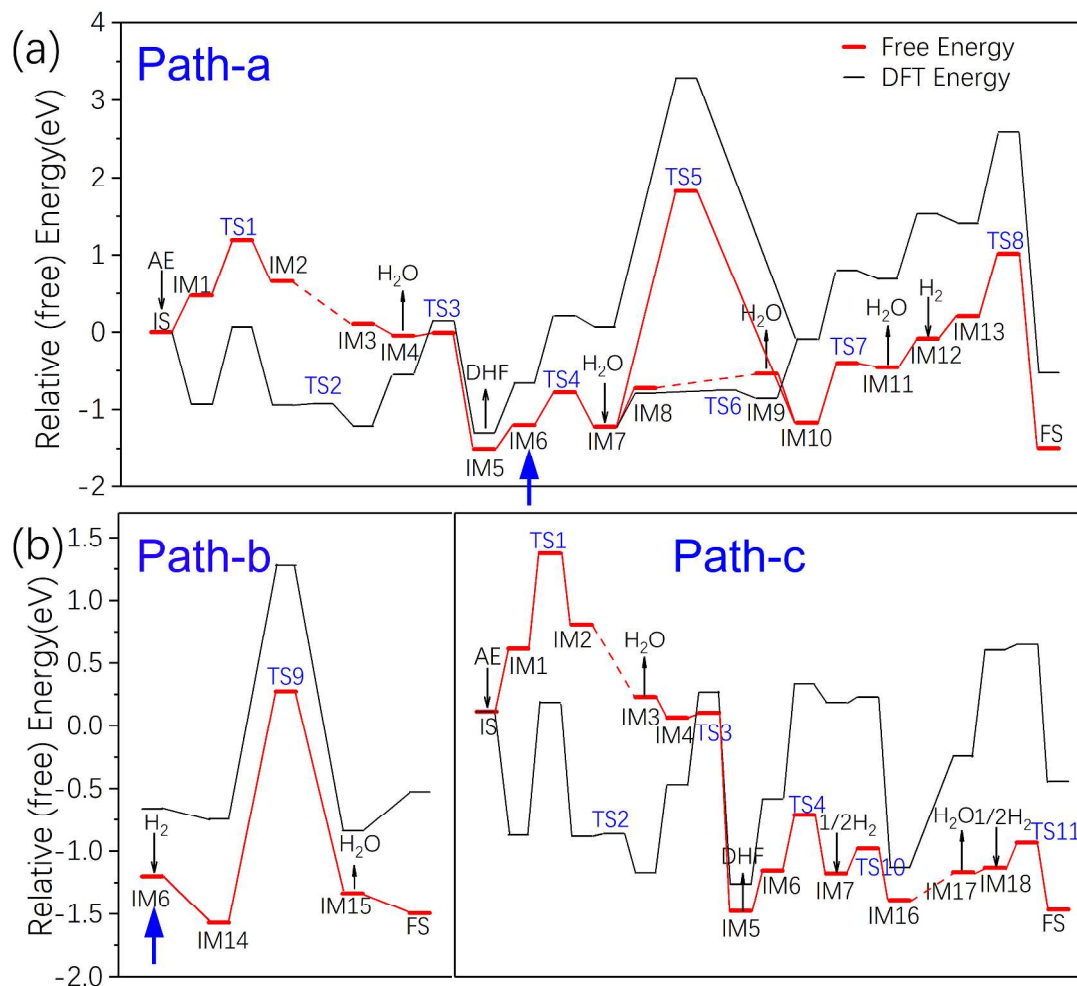
Figure 4. Energy profiles of AE DODH reaction over ReO/CeO$_2$ using **Model-A**. **a.** Surface hydrogen migration mechanism with the hydrogen vacancies replenished by dissociation of H$_2$. **b.** Direct reduction of ReO$_2$ by H$_2$. **c.** Surface hydrogen migration mechanism with atomic hydrogen assumed to be abundant. IS, IM and FS denote initial state, intermediate state and final state, respectively. Red dashed line denotes that the free energy barrier (T = 413 K and experimental partial pressures given in section 2) of an elementary step vanishes (e.g. **IM2→IM3**). For **IM16→IM17**, the DFT energy barrier vanishes. The intermediate state where the reaction paths bifurcates is indicated by a blue arrow. The free energy of activation and reaction free energy are also provided in Table S1. A chemical formula description of all structures is given in Table S3.
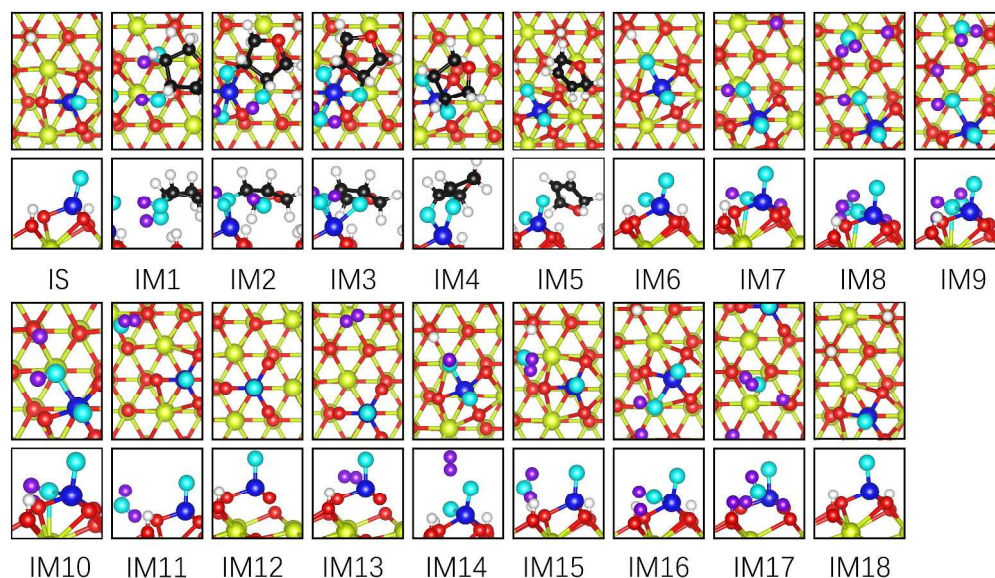
Figure 5. The structures (top view and side view) of initial state and intermediate states for the energy profiles in Figure 4. Black and purple balls denote carbon and hydrogen atoms, respectively. The other color patterns are the same as in Figure 1. A chemical formula description of all structures is also given in Table S2.

3.2 DODH reaction of AE over ReO/CeO$_2$

We computed the free energy profiles of the DODH reaction of AE over ReO/CeO$_2$ along with the surface hydrogen migration pathways, as displayed in Figure 4a. We report all energy barriers in free energy scale while the DFT energy profiles are also provided as a reference. The associated structures of initial/final states and intermediate states are presented in Figures 5 and S4 and Table S2. We found that an AE molecule adsorbs weakly on ReO/CeO$_2$, which is endergonic by 0.47 eV (**Path-a**). In the adsorbed state (**IM1**), one hydrogen of the hydroxyl group of AE binds through a hydrogen bond with the protruding oxygen of ReO. This hydrogen then forms a chemical bond with the Re oxygen, concomitant with formation of another Re-O bond. The first O-H bond-breaking forms **IM2** which involves overcoming a free energy barrier of 0.72 eV (all reported activation energies are on a free energy scale unless stated otherwise). The breaking of the second O-H is accompanied with the formation of H$_2$O and a Re-O bond. This step was found to be barrierless, which can be attributed to the close vicinity of the AE hydrogen with the Re-bonded OH and thus, the strong tendency to form a H$_2$O in **IM3**. The formed H$_2$O can desorb readily, forming **IM4**. Next, C-O bond-breaking can occur readily with a free energy barrier of 0.05 eV(**IM4→IM5**), followed by the desorption of the physisorbed DHF (**IM5→IM6**). The formed

13

ReO_2 state (**IM6**) is then allowed to be reduced by the hydroxyl-hydrogen on ceria. The steps of **IM6→IM7** and **IM7→IM10** correspond to the steps d and e in Figure 3. Consistent with a previous computational study that hydrogen migration on CeO_2 has a high barrier,[51] the energy barrier of step **IM7→IM10** is 3.04 eV in our study. Owing to the insurmountable barrier of direct hydrogen migration, we also considered the water-assisted surface hydrogen migration, or a so-called Grotthus mechanism, which has a significantly reduced activation energy.[52, 53] Indeed, we found that the free energy barrier of hydrogen migration in the presence of water (**IM8→IM9**) vanishes and the activation energy was assigned to be the endergonicity of the forward reaction (0.19 eV). The ReO_2 reduction process is completed in **IM10→IM11**. Then, the formed water desorbs readily, leaving two hydrogen vacancies on the hydroxylated ReO/CeO_2 surface, which should be replenished in the ensuing steps. In the present case, however, the dissociation of H_2 on CeO_2 (**IM13→FS**) has a high energy barrier of 0.81 eV. For comparison, we also examined the direct reduction of ReO_2 by hydrogen, which has an energy barrier of 1.85 eV (**IM14→IM15** in Figure 4b, **Path-b**). Considering the energy of **TS8** relative to **IM6** is 2.22 eV and is even larger than the energy barrier of **IM14→IM15**, the surface hydrogen migration process has a higher effective barrier than the direct reduction process and the latter is mainly responsible for the reduction of ReO_2. If the dissociation of H_2 is facile and the hydrogen vacancies can be replenished readily (e.g. through hydrogen spillover), another surface hydrogen migration process, whereby ReOOH species is involved (Figure 4c, **Path-c**), is also made feasible. In this case, we also assume that the dissociation of H_2 is independent of the reactions occurring near ReO/ReO_2 and that replenishment of one H_{vac} by 1/2 H_2 in **IM7** has only an activation energy of the water-assisted hydrogen migration on CeO_2 (0.19 eV). The reaction then takes place between the Re-bonded OH and the hydrogen of the surface hydroxyl (**IM16→IM17**), which is followed by the replenishment of the newly formed H_{vac} (**IM18→FS**). To this end, the catalytic cycle is also complete. The effective barrier of ReO_2 reduction along **Path-c** is only 0.72 eV. Briefly, the reactions of **Path-a** and **b** take place over pristine ReO/ReO_2, for which the energy profiles are not favorable, while a more favorable **Path-c** is feasible only when the replenishment of H_{vac} can readily occur (due to the presence of e.g. a Pd site close-by).
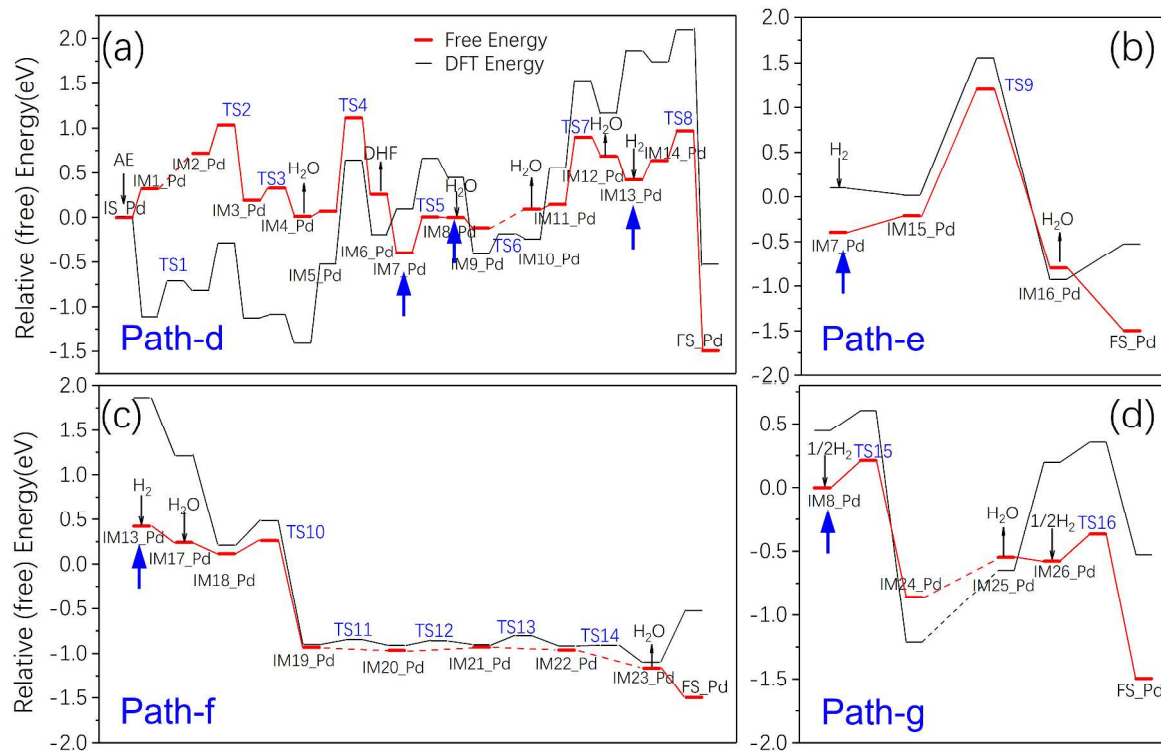
Figure 6. (Free) energy profiles of AE DODH reaction over ReO-Pd/CeO$_2$ using **Model-B** (T = 413 K and experimental partial pressures given in section 2.). **a.** Surface hydrogen migration mechanism with the hydrogen vacancies replenished by dissociation of H$_2$ on a ceria site. **b.** Direct reduction of ReO$_2$ by H$_2$. **c.** The two hydrogen vacancies of **IM13_Pd** replenished through hydrogen spillover from Pd$_4$ onto CeO$_2$ **d.** Hydrogen vacancy of **IM8_Pd** replenished through surface hydrogen migration mechanism with atomic hydrogen assumed to be abundant (equivalent scenario to Path-c but with the presence of a Pd cluster). The _Pd extension for all transition states are omitted for brevity. The intermediate states where the reaction paths bifurcate are indicated by blue arrows. The free energy of activation and reaction free energy are also provided in Table S2. A chemical formula description of all structures is given in Table S3.
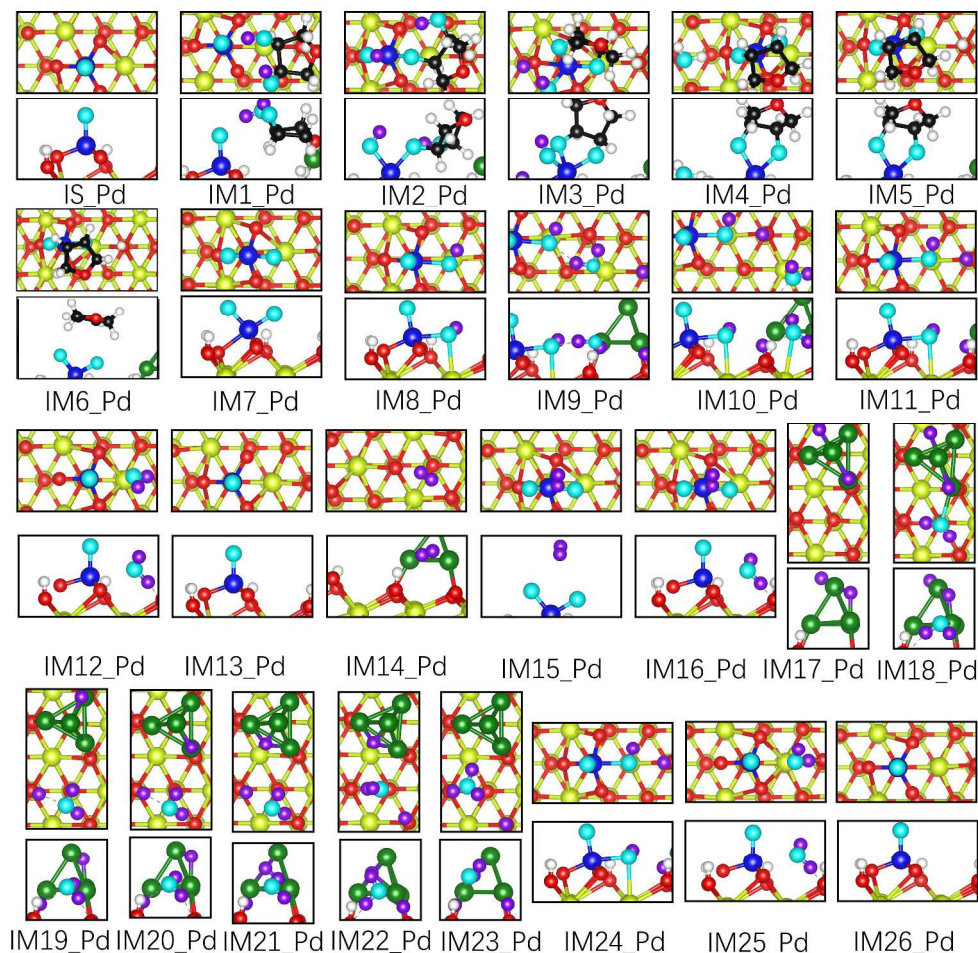
Figure 7. The structures (top and side view) of initial state and intermediate states for the energy profiles in Figure 6.

3.3 DODH reaction of AE over ReO-Pd/CeO$_2$

Consistent with experimental observations, our computational results suggest that the DODH of AE over ReO/CeO$_2$ has a low activity. We next investigated the reaction over ReO-Pd/CeO$_2$ with **Model-B** and the energy profile is displayed in Figure 6, corresponding to the surface hydrogen migration mechanism where the hydrogen vacancies are replenished by dissociation of H$_2$ on a ceria site(**Path-d**), ReO$_2$ reduced directely by H$_2$ molecule(**Path-e**), the hydrgeon spillover from Pd cluster onto ceria and the replenishment of H vacancy(**Path-f**) and H vacancy replenishment through surface hydrogen migration mechanism with atomic hydrogen assumed to be abundant(**Path-g**). The associated structures of the initial, intermediate, and final states are presented in Figure 7 and Figure S5. The scission of the first O-H

bond for AE has a barrier of 0.40 eV (**IM1_Pd→IM2_Pd**), lower than that for ReO/CeO$_2$ (**Path-d**). In the second O-H scission step (**IM2_Pd→IM3_Pd**), the hydrogen originally belonging to the Re-bonded OH migrates to an oxygen pertaining to the CeO$_2$ substrate, while the Re-bonded OH returns immediately after accepting the hydrogen from the second OH of AE, concomitant with the formation of a new Re-O bond. Subsequently, a H$_2$O molecule is formed, followed by the desorption of H$_2$O and DHF. The second O-H bond breaking of AE over ReO-Pd/CeO$_2$ has an effective barrier of 1.03 eV (**TS2_Pd** relative to **IS_Pd**), lower than the effective barrier of 1.18 eV for ReO/CeO$_2$ (**TS1** relative to **IS** in Figure 4a), which is indicative of a more facile DODH over ReO-Pd/CeO$_2$. The DHF formation step (**IM5_Pd→IM6_Pd**) has a barrier of 1.05 eV and the effective barrier of **TS4_Pd** is 1.11 eV. As compared with the ReO/CeO$_2$ counterpart, the high barrier can be explained by the fact that C-O bond breaking over ReO-Pd/CeO$_2$ is endergonic by 0.20 eV while that of ReO/CeO$_2$ is exergonic by 1.51 eV.

Similar to the reaction over ReO/CeO$_2$, the reduction of the ReO$_2$ species for ReO-Pd/CeO$_2$ in **IM7_Pd** also involves a surface hydrogen migration process and subsequent replenishment of hydrogen vacancies. Here, only the water-facilitated hydrogen migration was considered. **TS7_Pd**, corresponding to the transition state of the water formation by reducing ReO$_2$, is 1.29 eV above **IM7_Pd** in the free energy diagram. Physisorption of H$_2$ on **IM13** is endergonic by 0.22 eV and the dissociation of H$_2$ on ReO-Pd/CeO$_2$ (**IM14_Pd→FS_Pd**) has a barrier of 0.33 eV. The low barrier of H$_2$ dissociation is likely related to the interaction between the two hydrogen vacancies and the neighboring Pd$_4$ cluster. Overall, the effective barrier of ReO$_2$ reduction along **Path-d** is 1.37 eV. The direct reduction of ReO$_2$ by hydrogen for ReO-Pd/CeO$_2$ (**IM15_Pd→IM16_Pd** in **Path-e**, Figure 6b) has a barrier of 1.42 eV. The reduced barrier, as compared with the ReO/CeO$_2$ counterpart, can be attributed to the higher exergonicity of ReO$_2$ reduction for ReO-Pd/CeO$_2$ (-0.94 eV) than for the ReO/CeO$_2$ catalyst model (0.24 eV, **IM14→IM15** in **Path-b**).

In the presence of a co-adsorbed Pd cluster, the replenishment of the two hydrogen vacancies can harness the facile dissociation of hydrogen on Pd.[54] Hence, we considered the hydrogen spillover from Pd$_4$ onto the CeO$_2$ support (Figure 6c, **Path-f**). The dissociative adsorption of a H$_2$ molecule on Pd$_4$ is barrierless and **IM13_Pd→IM17_Pd** was treated as an adsorption process. In the hydrogen spillover

process, a hydrogen migration on CeO_2 is needed; therefore, we introduced a pre-adsorbed water that has been proven to facilitate hydrogen migration. The H_2O molecule is stabilized by Pd_4 (**IM18_Pd**). Due to the close vicinity of H and H_2O, the first hydrogen migration from Pd_4 to CeO_2 (**IM18_Pd→IM19_Pd**) is passed on by water, following a Grotthus mechanism and replenishing a H_{vac}. Subsequently, the other hydrogen diffuses for two steps on the Pd_4 cluster to be in a favorable position for spillover onto CeO_2 (**IM19_Pd→IM20_Pd→IM21_Pd**). Then, the migration of hydrogen to a second H_{vac} is assisted by water (**IM21_Pd→IM22_Pd**) and the newly formed H_{vac} is replenished by hydrogen from the Pd_4 cluster (**IM22_Pd→IM23_Pd**). Finally, the added water desorbs and the hydrogen spillover process is completed. The hydrogen spillover mechanism has very favorable kinetics, for which **IM18_Pd→IM19_Pd** has a barrier of only 0.15 eV, while the other barriers vanish in the free energy scale. Comparing the energy profiles of **Path-d**, **e** and **f**, we conclude that the hydrogen spillover mechanism is mainly responsible for the replenishment of hydrogen vacancies during the catalyst regeneration process.

Since the replenishment of hydrogen over ReO-Pd/CeO_2 is facile, it is reasonable to expect the reaction to occur following the surface hydrogen migration mechanism (**Path-g**, Figure 6d), with one H_{vac} replenished by "1/2 H_2" and involvement of a ReO(OH) species (**IM24_Pd**, Figure 7), which has an effective barrier of 0.41 eV. **Path-c** also becomes a possible process when a co-adsorbed Pd cluster on ceria is far away from the catalytic Re center, which does not alter the reactivity of the DODH, yet catalyzes the H_{vac} replenishment process.

3.4 Microkinetic modelling

Having established the energy profiles of each reaction, we developed MKMs for various reaction mechanisms for the DODH over the two catalysts and determined the degree of rate control under experimental reaction conditions. The MKM of the overall process for **Path-a** and **b** suggests that its TOF at 413 K is 1.47×10^{-10}/s. The calculated vanishingly small TOF is qualitatively consistent with the experimental fact that the activity of the catalyst is low in the absence of any transition metal promoter. Although most of the Re exists in monomeric form in the prepared catalyst, there is some degree of agglomeration of a small portion of Re, which can contribute to a hydrogen spillover pathway and a TOF

higher than the one calculated here. The KRC of **TS9** approaches 1, suggesting that the kinetics of the DODH over Re/CeO$_2$ is controlled by the direct reduction of the ReO$_2$ species. When the reaction proceeds along **Path-c** for which the replenishment of H$_{vac}$ can readily occur, the TOF dramatically increases to 4.33×10^{-3}/s. The reaction kinetics is controlled by **TS1** whose KRC approaches 1. Here, the TRC of IM5 is -0.82, suggesting that destabilization of the DHF adsorbed state (IM5) leads to an increase in TOF. The overall TOF for **Path-d**, **g**, **e** and **f** was found to be 9.90×10^{-2}/s. Unlike **Path-c**, the kinetics for the overall process of **Path-d**, **g**, **e** and **f** is primarily controlled by the C-O bond dissociation process (**TS4_Pd**) with a KRC of 0.93. In addition, the energy of the intermediate state IM4_Pd and the initial state IS_Pd have a significant effect on the reaction rate with TRC values of -1 and -0.44, respectively. The effective barrier of **TS1** in **Path-c** is 0.07 eV higher than **TS4_Pd** in **Path-d**, which explains the lower activity (TOF) of **Path-c**. As such, we can conclude that the roles of co-adsorbed Pd in ReO-Pd/CeO$_2$ are twofold: (a) Pd catalyzes the hydrogen spillover onto ceria, which enables the surface hydrogen migration process through **Path-g** and (b) Pd facilitates the breaking of AE O-H bonds on Re sites. However, it renders the C-O bond breaking more difficult than the absence of it. In other words, the effect of Pd is fully "turned on" for the reactions of **Path-d**, **g**, **e** and **f** while it only behaves as a hydrogen spillover catalyst for **Path-c**, representing two limiting cases.

The experimental TOF was reported at 443 K as 0.083/s[20] for ReO-Pd/CeO$_2$, while we obtained a higher TOF of 0.42/s under the same condition with our MKM. We note that the predicted TOF is for the DODH process while the experimentally measured value is for the consecutive process of DODH and the hydrogenation of DHF. Considering that the Pd-ceria interaction in the experiments is likely in-between the above-mentioned limiting cases and that underestimating the activation energy of the rate-determining step by only 1 kcal/mol leads to a factor ~3 decrease in TOF, we consider the predicted TOF to be in very good agreement with the experimental value.

The apparent activation energies, E$_{app}$, of **Path-c**, as well as the overall process of **Path-d**, **e**, **f** and **g** were obtained within the temperature range of 383 to 443 K using an Arrhenius plot (Figure S6). The respective E$_{app}$ were found to be 1.13eV and 1.15 eV, respectively. Particularly for **Model-B** (**Path-d, e, f, and g**), we observe a non-linear Arrhenius plot with a lower activation barrier at higher temperatures. The

non-linearity can be explained by a decreasing importance of the product desoption process (C-O bond cleavages – **TS4_Pd**) with increasing temperature and a corresponding increase in importance of the initial O-H dissociation process (**TS2_Pd**). Specifically, the KRC of **TS4_Pd** decreases from 0.99 to 0.75 when increasing the temperature from 383 K to 443 K (i.e., the KRC of **TS2_Pd** increases from practically zero to 0.25). Considering that the energy barrier of the reaction involving **TS2_Pd** possesses a lower energy barrier than the one from **TS4_Pd**, the Arrhenius plot curves to lower values with increases temperature.

Next, the reaction order (α_i) with respect to H_2 was found to be 0, consistent with prior experimental results. With respect to the AE concentration, we found (consistent with the rate controlling steps for the models) a reaction order of 1 for **Model-A** and 0.5 for **Model-B**. Both reaction orders are somewhat consistent with prior experimental results that observed a decreasing AE reaction order with AE concentration. Finally, it should be mentioned that a water solvent is unfavorable for the DODH reaction, a MKM with a H_2O pressure of 3.56 bar (water solvent condition) predicts for **Path-c** an over one order of magnitude lower TOF (1.12×10^{-4}/s) as with a H_2O pressure of 0.08 bar (4.33×10^{-3}/s). The reduction in TOF can be understood by the higher stability of the ReO(OH) species relative to ReO at higher oxygen chemical potential in water (see Figure S3), reducing the number of active Re sites. For **Path-d**, **e**, **f** and **g**, the computed TOF at a H_2O pressure of 3.56 bar is 2.52×10^{-3}/s (versus 9.90×10^{-2}/s at low water chemical potential). The reduction in TOF can be explained by the free energy of **TS4_Pd** being increased by 0.13 eV relative to the initial state due to the change in H_2O chemical potential.

3.5 Electronic interaction between CeO_2 and the supported species

So far, we have demonstrated a high catalytic activity of the ReO-Pd/CeO_2 catalyst system for the DODH reaction. As their seems to be some medium-range communication between nearby (but not in direct contact) Pd and ReO_x sites in the ReO-Pd/CeO_2 catalyst, we analyze the electronic interaction between CeO_2 and the supported species to provide insight into the promotional effect of Pd. Intuitively, ReO and the Pd_4 cluster tend to donate electrons to the f-orbital of Ce, reducing some Ce^{4+} to Ce^{3+}. We employ the site-specific magnetic moment as a measure of the oxidation state (OS) of Re and Ce. The existence of Ce^{3+} is characterized by a f-electron magnetic moment of approximately 1 and the

spin-density localized on Ce atoms (Figure 8). The d-orbital magnetic moment, the Bader charge and the OS of Re, as well as the number of Ce^{3+} in our catalyst model are summarized in Table 1. It should be mentioned that the calculated magnetic moment of Re(VI) is ca. 0.6 μ_B which is less than 1 μ_B due to electron over-delocalization typical of DFT. For Re(VII), the d-orbital magnetic moment approaches 0. The difference in OS of different Re species is also confirmed by Bader charge analysis (see Table 1). The spin density of adsorbed ReO and Pd_4 on both the pristine $CeO_2(111)$ surface and the hydroxylated surface are visualized in Figure 8. On pristine $CeO_2(111)$, 5 Ce^{4+} were found to be reduced by the ReO species (Figure 8a), for which Re reaches its highest oxidation state of +7. In contrast, there is essentially no charge transfer between the Pd_4 and $CeO_2(111)$ (Figure 8b). In the presence of both ReO and Pd_4 (Figure 8c), 6 Ce-ions are reduced. On the OH-terminated/hydroxylated $CeO_2(111)$ surface, each H atom donates one electron to $CeO_2(111)$, reducing the surface ceria atoms. Specifically, we found that 13 Ce^{4+} (all 12 surface Ce^{4+} and 1 subsurface Ce^{4+}) are reduced for ReO on the hydroxylated ceria surface (Figure 8d). Considering the contribution of the 9 surface H atoms, the ReO species donates 4 electrons and the OS of Re is assigned to be +6. The d-z^2 like spin density localized on the Re(VI) is illustrated in Figure 8d. To confirm our DFT+U calculations, we also performed single-point calculations of ReO(hy) using the HSE06 functional. Again, we found a Re d-orbital magnetic moment of 0.65 μ_B and 13 reduced Ce^{3+} ions. To understand the high OS of Re under the experimental reaction conditions (which are reducing), we realize that ceria can easily be reduced by adsorbed species such as Re that is stable in a +6 and +7 oxidation state but relatively unstable in a +5 OS. Also, the reduction of sub-surface Ce ions is more difficult than the reduction of surface Ce ions such that the Re species is only able to reduce one sub-surface Ce ion.

To better understand the interaction between the reduced ceria support and the ReO species, we removed up to three H atoms from the ReO model supported on a hydroxylated ceria surface (Figure 8e,f,g). In the case of one H vacancy, the number of electrons transferred to the Ce-ions is 12 (, i.e., all surface Ce-ions are reduced) and Re remains in a +6 state. Upon the removal of an additional H atom from the ceria surface, the electron affinity of the surface Ce-ions is strong enough to further oxidize Re. Note in Figure 8f that the d-electron magnetic moment of Re is non-vanishing, therefore we assign a 7-δ

OS to Re (δ is a small positive number). Further removal of a third H atom (Figure 8g) from the ceria surface leads to 11 Ce-ions being reduced, i.e., Re is in its highest possible oxidation state and it cannot donate any additional electrons to the ceria surface.

Next, we found that a Pd_4 cluster adsorbed on a hydroxylated CeO_2 surface donates 1 electron (Figure 8j), consistent with that on the pristine surface. When both ReO and a Pd_4 cluster are coadsorbed on the hydroxylated CeO_2 surface, the Pd_4 cluster donates 1 electron and the ReO species donates $5-\delta$ electrons to the hydroxylated CeO_2 surface, i.e., due to the presence of a nearby Pd_4 cluster, the OS of Re is increased from +6 to ca. +7. To confirm this form of medium-range communication between the Re and Pd sites, we calculated the Re d-orbital magnetic moment with the HSE06 functional and found a magnetic moment of 0.31 μ_B, which is again significantly lower than the one in the absence of the Pd_4 cluster. Pd-ReO(hy) core level shift[55] calculations suggest that the Re 4f level binding energy for Pd-ReO(hy) is 0.72 eV higher than that of the same catalyst model in the absence of the Pd cluster, corroborating the higher OS of the former case. The origin for the different OS of Re between ReO(hy) and Pd-ReO(hy) is that 3 surface H atoms can donate 3 electrons while Pd_4 only donates 1 electron to CeO_2 (i.e., the Pd cluster donates fewer electrons than the surface H atoms that would be present in the absence of the Pd cluster). Also the electron donation from ReO to CeO_2 is "nonlocal" (i.e. not just the Ce_3 triangle directly underneath ReO are reduced, which is seen in Figure 8a). The nonlocal distribution of Ce^{3+} is consistent with previous studies which suggest that the two Ce^{3+} formed by removal of one oxygen on $CeO_2(111)$ surface are situated at non-neighbouring positions.[56, 57] Due to this nonlocality of electron donation, ReO tends to compensate the relatively poor electron-donation ability of the Pd cluster, leading to a high Re OS for Pd-ReO(hy). In this sense, the Pd cluster (even when not in direct contact with the Re-site) can be regarded as an oxidation state modifier of the Re-site via the CeO_2 substrate. The assignment of the Re OS for other key intermediates including ReO(OH) (Figure 8h,l) and ReO_2 (Figure 8i,m) on the reduced ceria surface along the reaction path, shown in Table 1, are all in agreement with the analysis above. To examine the interaction range between Re and Pd_4, we created a ($3\times4\sqrt{3}$) hydroxylated surface with Re and Pd_4 placed at a more distant position than that of the ($2\times4\sqrt{3}$) surface (Figure 8n). Here, the OS of Re is +6. Therefore, only one electron is transfered from the ReO region to the Pd_4 region

on CeO_2(111). It can be expected that a further increase of the distance between ReO and Pd_4 leads to the absence of electron transfer, resembling the case of ReO(hy) (Figure 8d). Overall, the extent to which Pd modifies the OS of Re is determined by their distance on CeO_2(111). The charge transfer process of CeO_2(111) supported Pd_4 and Re are schemisticlly displayed on Figure 9. In addition, the OS of Re for all reaction intermidates are provided in Table S3.

The difference in Re OS influences the energetics of the intermediate states and the activity of the catalyst system. Specifically, the energies of ReO_2 relative to ReO for the Pd_4-promoted system (**IM7_Pd** in **Path-d**) and the non-promoted system(**IM6** in **Path-a**) are 1.10 eV and 0.29 eV, respectively. Also, the ReO(OH) species in **Path-g** (**IM24_Pd**) is 0.64 eV higher in energy than ReO, while the counterpart of **Path-c** (**IM16**) is only 0.07 eV higher. The different energies of the reaction intermidates are responsible for the above-mentioned different activity of **Path-c** and the Pd-promoted case. Finally, we also considered the effect of adsorbed H on Pd_4 on the properties of Re. Figure S7 and Table S4 in the ESI show that the properties of Re are only marginally changed in the presence of pre-adsorbed hydrogen on the Pd cluster.

Up to now, our computational study is based on an ideal scenario with a small Pd cluster loaded on a stoichiometric CeO_2 (111) surface. It should be pointed out that the mechanism of the realistic DODH reaction catalyzed by ReO_x-Pd/CeO_2 is complicated by the presence of oxygen vacancies (OVs) on the ceria support, a size and facet effect of the CeO_2 support, and the surface coverage and ratio of ReO and Pd. We also mention here that the calculated OV formation free energy at 413K and a H_2 and H_2O partial pressure of 80 and 0.08 bar, respectively, is calculated to be 1.62 eV. The most stable OV is stabilized at sub-surface position.[56] Despite the fact that we compute a highly endergonic OV free energy, surface and subsurface OVs have been observed experimentally in ceria. [56] We therefore examined the effect of both surface and subsurface OVs on the electronic properties of Re in the absence/presence of Pd_4. Formation of a subsurface OV creates 2 Ce^{3+} while a surface OV creates 1 Ce^{3+} (since a OH group is removed to create the surface OV). Analysis of the spin densities (Figure 10) suggests that in all cases Re has a +6 OS. The calculated magnetic moment and Bader charge of Re are presented in Table 1. A schematics of charge transfer process for the case of co-adsorbed Re and Pd_4 in the presence of a sub-surface oxygen vacancy

is displayed in Figure 9d, corresponding to Figure 10 b and f. It appears that in the presence of oxygen vacancies even the Pd_4-containing system leads to a Re OS of +6 (instead of +7 in the absence of defects). Hence, the promotional effect of Pd only manifests itself as a hydrogen spillover catalyst and the above-mentioned promotional effect of changing the oxidation state of Re vanishes. In a recent experimental study, the catalytic activity of a ReO_x-Pd/CeO_2 is not sensitive to the distance between Re and the Pd cluster.[58] In other words, Pd only serves as H_2 spillover catalyst and the modification of the electronic properties of Re is less pronounced. This might be related to the presence of oxygen vacancies in CeO_2. To study the effect of Pd cluster size on the OS of Re, we repeated our oxidation state calculations for a Pd_{10} cluster on a pristine $CeO_2(111)$ surface (Figure S8). The Pd_{10} cluster, which occupies 6 oxygen sites, donates 2 electrons to the $CeO_2(111)$ support and for a model similar to **Model-B**, but with the Pd_4 cluster being replaced with Pd_{10}, the OS of Re is again +7. The overall effect of the adsorbed Pd metal cluster on the the coadsorbed Re species is determined by the distance between Re and the Pd cluster, the presence of oxygen vacancies and only to a lesser extent the size of the metal cluster.

Recently, a Au promoted ReO_x/CeO_2 catalyst has also been found to catalyze the DODH reaction using H_2 as reductant.[58, 59] To study how Au modifies the activity of a coadsorbed ReO active site, we replaced the Pd_4 cluster with a Au_4 cluster in our catalyst model (see Figure S9). Oxidation state calculations suggest that Au, unlike Pd, interacts weaker with the ceria support and cannot modify the Re oxidation state, i.e., the Re exhibits a +6 OS. Consequently, the key role of the Au cocatalyst in the ReO_x-Au/CeO_2 catalyst system appears to be the H_2 dissociation catalyzed by Au-ceria interface sites.[60] Based on both the experimental and computational results, we conclude that the facile activation of H_2 is a prerequisites for a DODH catalyst using H_2 as reductant. Otherwise, the ReO_x-support interaction determines (together with the reaction environment) the oxidation state of Re which can be further modified by select transition metals such as Pd. However, the oxidation state modification of Re by the transition metal is support defect dependent. Re(+6) is able to catalyze the DODH reaction and is likely the active site in the experimental catalysts. A Re(+7) is likely even more active than Re(+6) but it appears to be challenging to stabilize this Re species under reaction conditions.

Table 1. The d-electron magnetic moment(μ_B), the Bader charge and the OS of Re, as well as the number of reduced Ce-ions. (p) and (hy) denotes the prestine and hydroxylated ceria surface, respectively. H_v denotes a surface hydrogen "vacancy" on the hydroxylated ceria surface. Sub and top denote the position of the oxygen vacancy, i.e., if it is located in the subsurface or top layer, respectively.

Species	Magnetic moment of Re	Bader Charge of Re	OS of Re	Number of Ce^{3+}
ReO(p)	0.011	2.323	7	5
Pd(p)	NA	NA	NA	1
Pd-ReO(p)	0.031	2.368	7	6
ReO(hy)	0.577	2.187	6	13
ReO-1H_v(hy)	0.579	2.167	6	12
ReO-2H_v(hy)	0.135	2.414	7-δ	~12
ReO-3H_v(hy)	0.088	2.44	7	11
ReO(OH)(hy)	0.71	2.274	6	12
ReO_2(hy)	0.004	2.484	7	12
Pd(hy)	NA	NA	NA	10
Pd-ReO(hy)	0.165	2.372	7-δ	12
Pd-ReO(OH)(hy)	0.046	2.47	7	11
Pd-ReO_2(hy)	0.003	2.476	7	10
Pd-ReO_2(hy-double)	0.596	2.237	6	23
ReO(hy)-sub-OV	0.524	2.146	6	15
Pd-ReO(hy)-sub-OV	0.394	2.293	6+δ	13
ReO(hy)-top-OV	0.579	2.172	6	14
Pd-ReO(hy)-top-OV	0.508	2.233	6	12
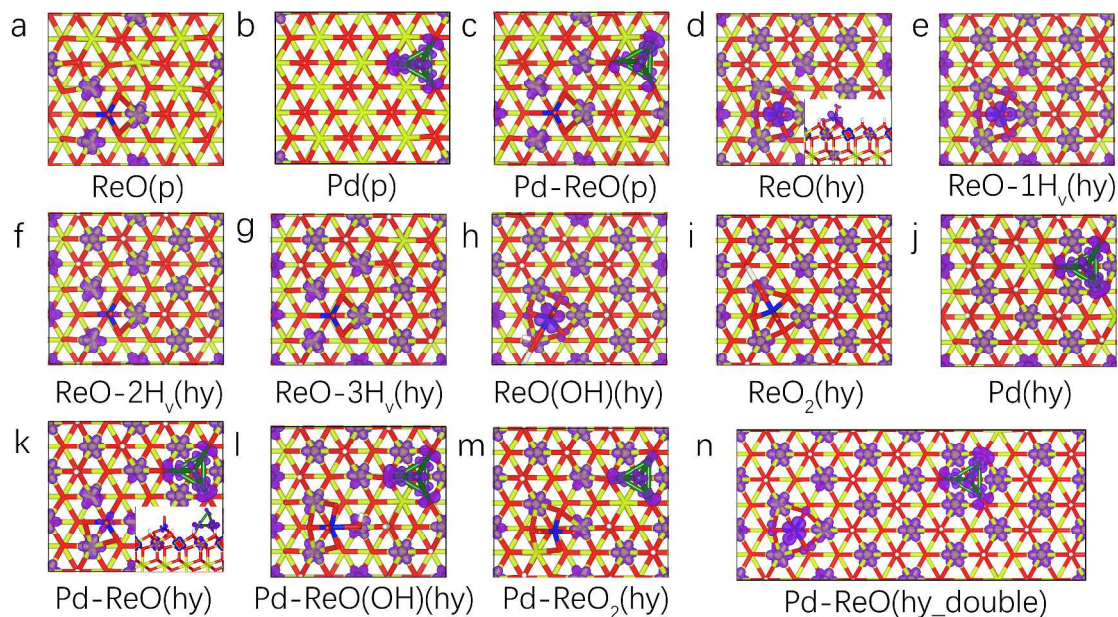
Figure 8. Spin density of ReO and Pd adsorbed on pristine (p) $CeO_2(111)$ (**a-c**) and surface hydroxylated (hy) $CeO_2(111)$ (**d-n**). The insets of **d** and **k** show the side views. The spin density isosurfaces are set to 0.01 e/$Å^3$. There can be anti-parallel spin of neighboring Ce^{3+} 4f electrons. Since we only consider the effect of charge transfer, the spin-ordering is not presented. It was found that energy difference between the ferromagnetical and antiferromagnetic states is less than 5 meV.[56]
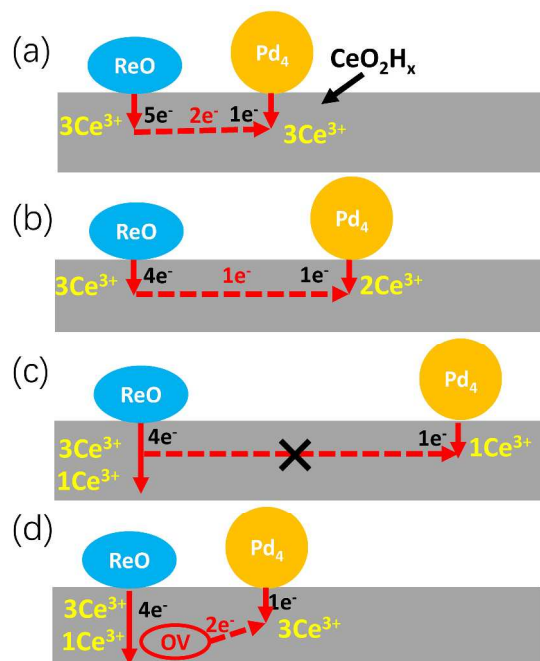
Figure 9. Charge transfer process of ReO and Pd$_4$ on a hydroxylated CeO$_2$(111) surface. **a.** short distance, **b**. medium distance **c.** long distance between the ReO and Pd$_4$ site. **d**. Effect of an oxygen vancancy on charge transfer (the case of Figure 10 b, f).
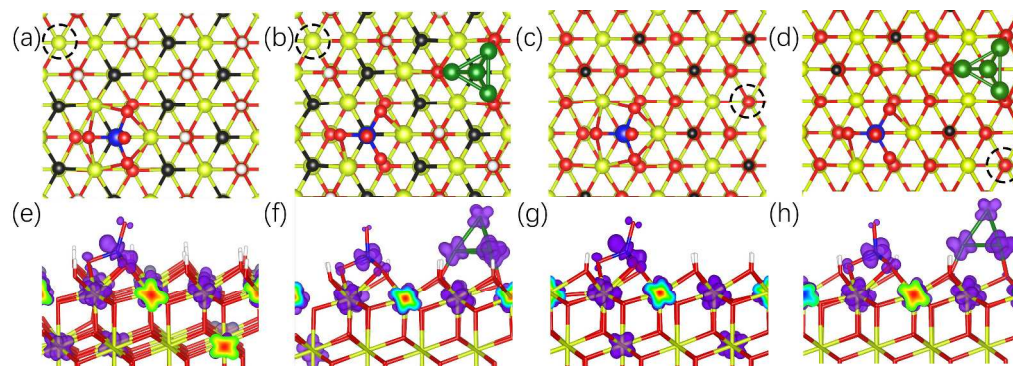
Figure 10. ReO and Pd adsorbed on CeO$_2$(111) with a subsurface oxygen vacancy (**a**, **b**) and surface oxygen vacancy (**c**, **d**). The subsurface oxygen is highlighted as a black ball and the position of the most stable oxygen vacancy site is indicated by a black circle (**a**, **b**). An OH group is removed to create a surface oxygen vacancy. The surface hydrogen is highlighted as black(**c**, **d**). The spin densities of **e**, **f**, **g**, **h** correspond to **a**, **b**, **c** and **d**, respectively.

4. Conclusions

We performed first principles calculations to understand the deoxydehydration of 1,4-anhydroerythritol (AE) on ReO/CeO$_2$ and ReO-Pd/CeO$_2$ catalysts. We started from an ideal support model without oxygen vancancies and a CeO$_2$(111) facet. Ab initio thermodynamic calculations suggest that the ceria surface is fully-hydroxylated while the structure of the ceria supported Re species is ReO. The established atomistic structures were used to examine the mechanism of the AE deoxydehydration. The removal of the two AE OH groups takes place at a ReO site, converting it to a ReO$_2$ species. The direct reduction of ReO$_2$ by H$_2$ was found to be difficult. Therefore, we proposed an alternative water-facilitated surface hydrogen migration mechanism, which creates two hydrogen vacancies on the hydroxylated surface. For the ReO/CeO$_2$ catalyst model the replenishment of hydrogen vacancies through dissociative adsorption of H$_2$ needs to overcome a very high barrier and the direct reduction of ReO$_2$ remains the dominant (but slow) pathway. In the presence of a co-adsorbed Pd cluster near the ReO/CeO$_2$, the replenishment of hydrogen vacancies is facile due to rapid hydrogen spillover from the Pd cluster onto the CeO$_2$ surface. In this context, we identified a pathway involving a ReO(OH) species that is highly

efficient for the reduction of ReO$_2$. To disentangle the specific contributions of Pd in the multicomponent catalyst, we investigated a hypothetical case where Pd only catalyzes the replenishment of hydrogen vacancies after a water-facilitated surface hydrogen migration process, i.e., it is assumed that the properties of the Re species are unaltered since the Pd is far away. This scenario leads to a high DODH activity in a non-aqueous solvent. The activity in liquid water is reduced due to a reduction in the number of active sites at a higher oxygen chemical potential. When Pd is in close proximity to the Re site (but not in direct contact), a MKM suggests a TOF at 413 K for ReO-Pd/CeO$_2$ that is higher than the one in the ideal case. The increase in activity originates from nearby Pd modifying the oxidation state of Re from +6 to +7, leading to a more facile O-H bond breaking process. The DHF removal was found to be the rate-limiting step for ReO-Pd/CeO$_2$ (**TS4_Pd**), different from the case where Pd only serves as a hydrogen spillover catalyst whose rate-limiting step is the O-H bond breaking (**TS1**). The effective barrier of **TS4_Pd** is 0.07 eV lower than **TS1**, leading to the higher TOF of the former reaction path. It should be noted that even in the absence of the promotional effect of Pd, we still predicted an appreciable TOF of 4.33×10^{-3}/s at 413K.

To better account for the properties of an experimental catalyst containing defects, we investigated the effect of oxygen vacancies. In the presene of OV, Re tends to exhibit an OS of +6, mimicking the properties of the above-mentioned hypothetical case. The key role of Pd is to dissociate hydrogen and function as a hydrogen spillover catalyst on the ceria surface. Without the continuous supply of surface hydrogen atoms the Re site cannot be regenerated, i.e., the catalytic cycle cannot be closed, and the TOF for the DODH is vanishingly small. When considering the effect of oxygen vacancies on the ceria support, our computational results are consistent with recent experimental observations.

Overall, the combination of oxide support, defects, and nearby metal cluster determine the oxidation state and activity of the Re species. Considering that we find that the DODH activity could be improved if a Re(+7) species could be stabilized (rather than the already active Re(+6) species), there might be room for further improvements of DODH catalysts based on single Re sites.

Electronic supplementary information

Slab Model, Gibbs free energies of ReO$_x$(OH)$_y$ species relative to ReO$_3$ at high water partial pressure,

partial pressure estimation of anhydroerythritol and dihydrofuran, labelling of selected bond lengths, formulation of harmonic transition state theory, energetics, free energies, and rate constants of all elementary steps, apparent activation energy calculations, the effect of pre-adsorbed hydrogen on the properties of Re, atomic coordinates of all interdimate and tranision states along reaction pathwas (in VASP format). Matrices for solving the master equations is provided as supplementary datasheet.

Author information

Corresponding Author

*E-mail for A.H.: heyden@cec.sc.edu.

Notes

The authors declare no competing financial interest.

Acknowledgments

References

1.   A. Corma, S. Iborra and A. Velty, *Chem. Rev.*, 2007, **107**, 2411-2502.
2.   J. Q. Bond, D. M. Alonso, D. Wang, R. M. West and J. A. Dumesic, *Science*, 2010, **327**, 1110-1114.
3.   H. Wang, Q. Kong, Y. Wang, T. Deng, C. Chen, X. Hou and Y. Zhu, *ChemCatChem*, 2014, **6**, 728-732.
4.   O. Mamun, E. Walker, M. Faheem, J. Q. Bond and A. Heyden, *ACS Catal.*, 2016, **7**, 215-228.
5.   S. Maetani, T. Fukuyama, N. Suzuki, D. Ishihara and I. Ryu, *Chem. Commun.*, 2012, **48**, 2552-2554.
6.   J. Lu, M. Faheem, S. Behtash and A. Heyden, *J. Catal.*, 2015, **324**, 14-24.
7.   A. R. Petersen and P. Fristrup, *Chem. Eur. J.*, 2017, **23**, 10235-10243.
8.   G. K. Cook and M. A. Andrews, *J. Am. Chem. Soc.*, 1996, **118**, 9448-9449.
9.   J. E. Ziegler, M. J. Zdilla, A. J. Evans and M. M. Abu-Omar, *Inorg. Chem.*, 2009, **48**, 9998-10000.
10.   S. Liu, A. Senocak, J. L. Smeltz, L. Yang, B. Wegenhart, J. Yi, H. I. Kenttämaa, E. A. Ison and M. M. Abu-Omar,

Organometallics, 2013, **32**, 3210-3219.

11.   G. Chapman and K. M. Nicholas, *Chem. Commun.*, 2013, **49**, 8199-8201.

12.   J. R. Dethlefsen, D. Lupp, B.-C. Oh and P. Fristrup, *ChemSusChem*, 2014, **7**, 425-428.

13.   A. L. Denning, H. Dang, Z. Liu, K. M. Nicholas and F. C. Jentoft, *ChemCatChem*, 2013, **5**, 3567-3570.

14.   N. Ota, M. Tamura, Y. Nakagawa, K. Okumura and K. Tomishige, *ACS Catal.*, 2016, **6**, 3213-3226.

15.   L. Sandbrink, E. Klindtworth, H.-U. Islam, A. M. Beale and R. Palkovits, *ACS Catal.*, 2016, **6**, 677-680.

16.   L. Sandbrink, K. Beckerle, I. Meiners, R. Liffmann, K. Rahimi, J. Okuda and R. Palkovits, *ChemSusChem*, 2017, **10**, 1375-1379.

17.   I. Ahmad, G. Chapman and K. M. Nicholas, *Organometallics*, 2011, **30**, 2810-2818.

18.   C. Boucher-Jacobs and K. M. Nicholas, *ChemSusChem*, 2013, **6**, 597-599.

19.   T. V. Gopaladasu and K. M. Nicholas, *ACS Catal.*, 2016, **6**, 1901-1904.

20.   N. Ota, M. Tamura, Y. Nakagawa, K. Okumura and K. Tomishige, *Angew. Chem. Int. Ed.*, 2015, **54**, 1897-1900.

21.   B. E. Koel and J. Kim, in *Handbook of Heterogeneous Catalysis*, Wiley-VCH Verlag GmbH & Co. KGaA, 2008, DOI: 10.1002/9783527610044.hetcat0087.

22.   S. R. Bare, D. R. Strongin and G. A. Somorjai, *J. Phys. Chem.*, 1986, **90**, 4726-4729.

23.   S. J. Jenkins and D. A. King, *J. Am. Chem. Soc.*, 2000, **122**, 10610-10614.

24.   T. W. Hansen, J. B. Wagner, P. L. Hansen, S. Dahl, H. Topsøe and C. J. H. Jacobsen, *Science*, 2001, **294**, 1508-1510.

25.   D. Torres, F. Illas and R. M. Lambert, *J. Catal.*, 2008, **260**, 380-383.

26.   C. F. Huo, B. S. Wu, P. Gao, Y. Yang, Y. W. Li and H. Jiao, *Angew. Chem. Int. Ed.*, 2011, **50**, 7403-7406.

27.   T. C. R. Rocha, M. Hävecker, A. Knop-Gericke and R. Schlögl, *J. Catal.*, 2014, **312**, 12-16.

28.   C.-C. Yang, B. A. Kilos, D. G. Barton, E. Weitz and J. M. Notestein, *J. Catal.*, 2014, **319**, 211-219.

29.   Y. Lykhach, S. M. Kozlov, T. Skala, A. Tovt, V. Stetsovych, N. Tsud, F. Dvorak, V. Johanek, A. Neitzel, J. Myslivecek, S. Fabris, V. Matolin, K. M. Neyman and J. Libuda, *Nat Mater*, 2015, DOI: 10.1038/nmat4500.

30.   G. Kresse and J. Furthmuller, *Phys. Rev. B*, 1996, **54**, 11169.

31.   G. Kresse and J. Furthmuller, *Comput. Mater. Sci.*, 1996, **6**, 15-50.

32.   P. E. Blöchl, *Phys. Rev. B*, 1994, **50**, 17953-17979.

33.   G. Kresse and D. Joubert, *Phys. Rev. B*, 1999, **59**, 1758-1775.

34.   H. J. Monkhorst and J. D. Pack, *Phys. Rev. B*, 1976, **13**, 5188.

35.   M. Nolan, S. Grigoleit, D. C. Sayle, S. C. Parker and G. W. Watson, *Surf. Sci.*, 2005, **576**, 217-229.

36.   A. V. Krukau, O. A. Vydrov, A. F. Izmaylov and G. E. Scuseria, *J. Chem. Phys.*, 2006, **125**, 224106.

37.   S. Grimme, J. Antony, S. Ehrlich and H. Krieg, *J. Chem. Phys.*, 2010, **132**, 154104.

38.   G. Henkelman, B. P. Uberuaga and H. Jonsson, *J. Chem. Phys.*, 2000, **113**, 9901-9904.

39.   G. Henkelman and H. Jónsson, *J. Chem. Phys.*, 1999, **111**, 7010-7022.

40.   A. Heyden, A. T. Bell and F. J. Keil, *J. Chem. Phys.*, 2005, **123**, 224101.

41.   D. A. Siegel, W. C. Chueh, F. El Gabaly, K. F. McCarty, J. de la Figuera and M. Blanco-Rey, *J. Chem. Phys.*, 2013, **139**, 114703.

42.   M. Saleheen and A. Heyden, *ACS Catal.*, 2018, DOI: 10.1021/acscatal.7b04367, 2188-2194.

43.   S. Behtash, J. Lu, O. Mamun, C. T. Williams, J. R. Monnier and A. Heyden, *The Journal of Physical Chemistry C*, 2016, **120**, 2724-2736.

44.   S. Behtash, J. Lu, E. Walker, O. Mamun and A. Heyden, *J. Catal.*, 2016, **333**, 171-183.

45.   A. Schafer, A. Klamt, D. Sattel, J. C. W. Lohrenz and F. Eckert, *Phys. Chem. Chem. Phys.*, 2000, **2**, 2187-2193.

46.   G. Buzzi-Ferraris and F. Manenti, in *Computer Aided Chemical Engineering*, eds. I. D. L. Bogle and M. Fairweather, Elsevier, 2012, vol. 30, pp. 1312-1316.

47.   C. Stegelmann, A. Andreasen and C. T. Campbell, *J. Am. Chem. Soc.*, 2009, **131**, 8077-8082.

48.   S. Kozuch and S. Shaik, *J. Phys. Chem. A*, 2008, **112**, 6032-6041.

49.   F. R. Negreiros, M. F. Camellone and S. Fabris, *J. Phys. Chem. C*, 2015, **119**, 21567-21573.

50.   M. B. Watkins, A. S. Foster and A. L. Shluger, *J. Phys. Chem. C*, 2007, **111**, 15337-15341.

51.   D. Fernández-Torre, J. Carrasco, M. V. Ganduglia-Pirovano and R. Pérez, *J. Chem. Phys.*, 2014, **141**, 014703.

52.   L. R. Merte, G. Peng, R. Bechstein, F. Rieboldt, C. A. Farberow, L. C. Grabow, W. Kudernatsch, S. Wendt, E. Laegsgaard, M. Mavrikakis and F. Besenbacher, *Science*, 2012, **336**, 889-893.

53.   Y. Xi, Q. Zhang and H. Cheng, *J. Phys. Chem. C*, 2014, **118**, 494-501.

54.   C. Zhou, S. Yao, J. Wu, R. C. Forrey, L. Chen, A. Tachibana and H. Cheng, *Phys. Chem. Chem. Phys.*, 2008, **10**, 5445-5451.

55.   L. Köhler and G. Kresse, *Phys. Rev. B*, 2004, **70**, 165405.

56.   M. V. Ganduglia-Pirovano, J. L. F. Da Silva and J. Sauer, *Phys. Rev. Lett.*, 2009, **102**, 026101.

57.   H.-Y. Li, H.-F. Wang, X.-Q. Gong, Y.-L. Guo, Y. Guo, G. Lu and P. Hu, *Phys. Rev. B*, 2009, **79**, 193401.

58.   Y. Nakagawa, S. Tazawa, T. Wang, M. Tamura, N. Hiyoshi, K. Okumura and K. Tomishige, *ACS Catal.*, 2018, **8**, 584-595.

59.   S. Tazawa, N. Ota, M. Tamura, Y. Nakagawa, K. Okumura and K. Tomishige, *ACS Catal.*, 2016, **6**, 6393-6397.

60.   M. Pan, A. J. Brush, Z. D. Pozun, H. C. Ham, W.-Y. Yu, G. Henkelman, G. S. Hwang and C. B. Mullins, *Chem. Soc. Rev.*, 2013, **42**, 5002-5013.

TOC Figure